ARTICLE

# Charge Dynamics in Solution-Processed Nanocrystalline $CuInS_2$ Solar Cells

**Jonathan E. Halpert,[†,‡] Frederik S. F. Morgenstern,[†] Bruno Ehrler,[‡] Yana Vaynzof,[‡] Dan Credgington, and Neil C. Greenham***

Cavendish Laboratory, University of Cambridge, J.J. Thomson Avenue, Cambridge CB3 0HE, United Kingdom. [†]J.E.H. and F.S.F.M. contributed equally to this work. [‡]Present address: (J.E.H.) School of Chemical and Physical Sciences, Victoria University of Wellington, Gate 7, Kelburn Parade, Wellington, New Zealand 6012. (Y.V.) Centre for Advanced Materials, Heidelberg University, Im Neuenheimer Feld 227, 69120 Heidelberg, Germany. (B.E.) FOM Institute for Atomic and Molecular Physics (AMOLF), P.O. Box 41883, 1009 DB Amsterdam, The Netherlands.



## ABSTRACT

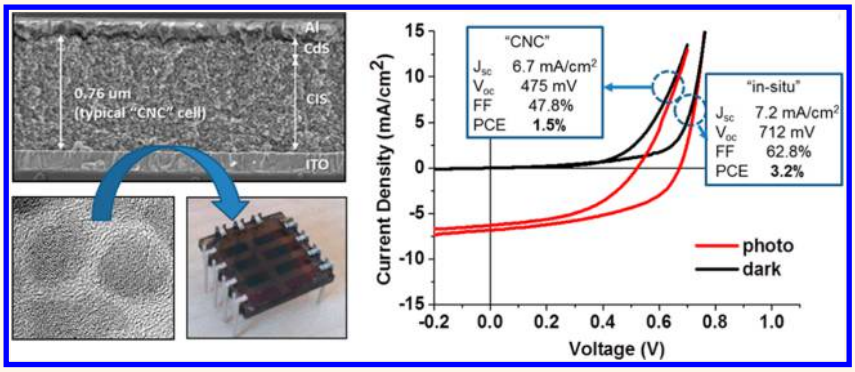


We investigate charge dynamics in solar cells constructed using solution-processed layers of $CuInS_2$ (CIS) nanocrystals (NCs) as the electron donor and CdS as the electron acceptor. By using time-resolved spectroscopic techniques, we are able to observe photoinduced absorptions that we attribute to the mobile hole carriers in the NC film. In combination with transient photocurrent and photovoltage measurements, we monitor charge dynamics on time scales from 300 fs to 1 ms. Carrier dynamics are investigated for devices with CIS layers composed of either colloidally synthesized 1,3-benzenedithiol-capped nanocrystals or *in situ* sol–gel synthesized thin films as the active layer. We find that deep trapping of holes in the colloidal NC cells is responsible for decreases in the open-circuit voltage and fill factor as compared to those of the sol–gel synthesized CIS/CdS cell.

**KEYWORDS:** nanocrystals · transient absorption · CIS · cupric chalcogenides · charge transfer · photovoltaics · quantum dot · trapping

Recent progress in the field of nanocrystal (NC) photovoltaics (PVs) has been driven by the need for solvent-dispersible, chemically robust materials to serve as the active layers in solar cells. Much of this interest has focused on materials currently being used in commercial thin-film photovoltaics, particularly cupric chalcogenides such as copper indium gallium sulfide/selenide (CIGS/Se),[1] copper indium sulfide/selenide (CIS/Se),[2] and copper zinc tin sulfide/selenide (CZTS).[3,4] However, the high-vacuum ($<10^{-5}$ mbar) and high-temperature (>400 °C) deposition methods needed to produce high-efficiency cells are either economically and energetically expensive or are incompatible with roll-to-roll processing onto common flexible substrates. Colloidally grown semiconductor nanocrystals could enable the use of low-temperature, scaleable atmospheric-pressure deposition methods such as inkjet printing or spray coating.[5−27] The main barrier to adoption of (non-sintered) cupric chalcogenide colloidal nanocrystal solar cells is their relatively low power conversion efficiencies (PCEs): generally less than 2% for most candidate materials, with the best devices achieving around 3%.[8] These are low with respect to both their thin-film analogues and lead-based nanocrystalline devices.[5,28−31] In the latter case, nearly a decade of work on the physics and conduction mechanisms present in these films has informed a series of incremental improvements in efficiency. Much less effort has been spent understanding the charge dynamics of devices using ternary and quaternary cupric chalcogenide nanocrystals.

* Address correspondence to ncg11@cam.ac.uk.

Received for review January 20, 2015 and accepted May 7, 2015.

**Published online May 07, 2015**
**10.1021/acsnano.5b00432**

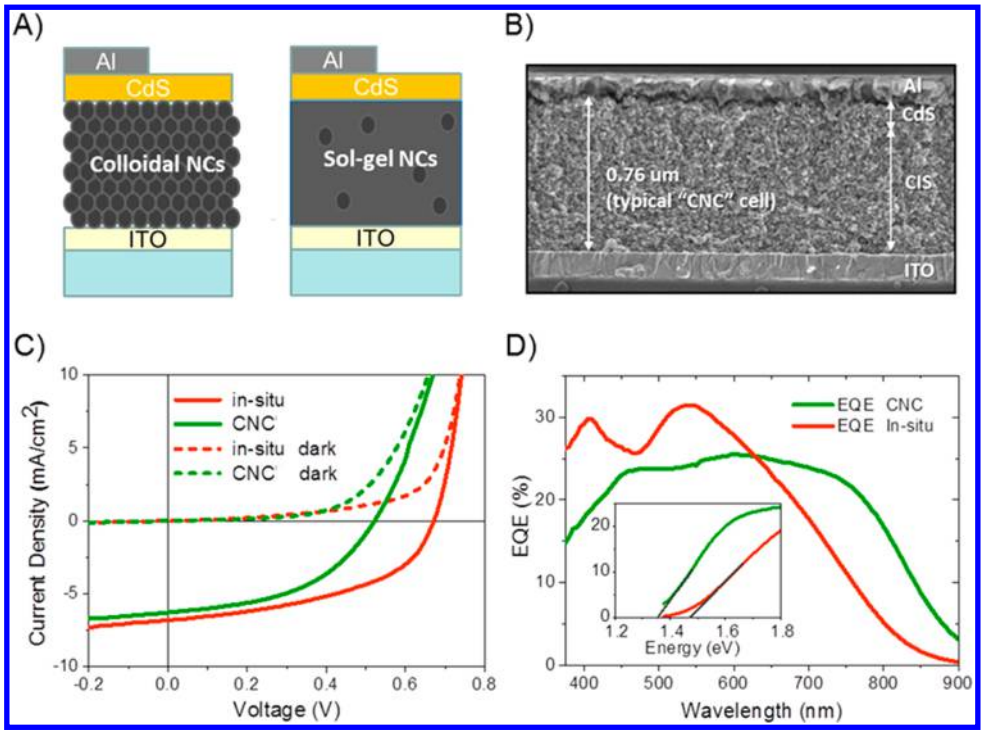


**Figure 1. (A) Diagram of a ITO/CIS/CdS/Al device using colloidal CIS nanocrystals (CNC). (B) Scanning electron microscope (SEM) image of the cross-section of a typical finished CNC device. (C) Current−voltage characteristics for devices using *in situ* and CNC CIS measured in the dark and under AM1.5 illumination. (D) External quantum efficiencies of *in situ* and CNC devices. The inset shows the same as a function of excitation energy. By linear extrapolation of the EQE curves, we obtain an estimate of the bandgap for CNC and *in situ* CIS of 1.35 and 1.47 eV, respectively (inset).**

## RESULTS AND DISCUSSION

Here, we study charge kinetics, recombination, and extraction in copper indium sulfide (CIS) solar cells coated with cadmium sulfide. We used solution-deposited CIS colloidal nanocrystals (CNCs) as the p-type absorber and hole transport material. Reference devices were prepared using sol−gel deposited (*in situ*) CIS produced by a previously reported method.[18] Sol−gel-deposited CdS is then used for both classes of device as an n-type electron transport material, which forms a type-II heterojunction with bulk CIS. Excited-state dynamics are observed on time scales of 300 fs to 1 ms using transient absorption spectroscopy. We obtain micro- to millisecond charge dynamics using transient photovoltage and photocurrent measurements. This allows us to track excited state and charge populations over a wide range of time scales, from immediately after excitation through charge separation and eventual collection at the electrode. Using this approach, we are able to infer the loss mechanisms contributing to lower PCE in colloidal nanocrystalline devices.

**Device Fabrication and Efficiency.** For the colloidal NC devices, spheroidal wurtzite nanocrystals with a bandgap of 1.49 eV were synthesized in oleylamine at 180 °C using a method adapted from those reported previously for CNC synthesis.[22,32,33] CNC films were fabricated using a layer-by-layer spin casting of purified nanocrystals from chloroform, alternating with spin coating of a 1,3-benzenedithiol linker (see Materials and Methods for more detail).

For comparison, we also prepared *in situ* grown NC thin film CIS/CdS solar cells using sol−gel methods adapted from Li et al.[18] The *in situ* CIS layer was produced by spin coating the CIS precursors with volatile ligand groups onto a substrate. Subsequently, the *in situ* film was annealed at 250 °C for 10 min, forming a thick film of mainly ligandless, nominally chalcopyrite particles with crystalline domains of size 1−10 nm.[18]

Approximately 50 nm of CdS was deposited on both *in situ* and CNC films as an electron-extracting layer (see Materials and Methods) by spin casting CdS precursors onto the substrate. The substrates were then annealed for 5 min at 250 °C to convert the precursor to bulk CdS.[18] One-hundred nanometers of aluminum was thermally evaporated through a shadow mask to form the top electrode, and devices were encapsulated under glass with an epoxy seal. Devices reported herein had an overall film thickness of ∼300 nm and an area of 4.5 $mm^2$.

A schematic representation of the device architecture is shown in Figure 1a. A scanning electron microscope (SEM) was used to image the cross-section of a typical finished CNC device (Figure 1b). PCE for the CNC CIS/CdS and *in situ* CIS devices was measured under 100 $mW/cm^2$ AM1.5G conditions and found to be 1.5 and 3.2%, respectively (Figure 1c). These values are comparable to previously reported devices of these

types.[8,18] CNC and *in situ* synthesized NC solar cells achieved similar short-circuit current densities ($J_{sc}$) of 6.7 and 7.2 mA/cm$^2$ and peak EQEs of 32 and 26%, respectively (Figure 1d). The main difference in PCE arises from a lower fill factor (FF) of 48% in CNC devices compared to 63% in their *in situ* counterparts, as well as a lower open-circuit voltage ($V_{oc}$) of 475 mV compared to 712 mV, respectively. Comparative device characteristics are summarized in Table 1.

The differences in external quantum efficiency (EQE) action spectra between the two device types can be accounted for by differences in the absorbance of the two films due to differences in NC particle size and variations in composition and crystallinity. UV−vis transmission measurements showed both CIS film types to be highly scattering, hindering a precise determination of their bandgap. However, by extrapolating their EQE response in the near IR as a proxy for the onset of absorption, we estimate the bandgaps of CNC and *in situ* devices to be 1.35 and 1.47 eV, respectively. The bandgap of cupric chalcogenides is particularly sensitive to differences in stoichiometry, and shifts in bandgap between 1.1 and 1.4 eV have been observed in $Cu_{2-x}S$.[34] The difference in bandgap of about ~0.1 eV, therefore, does not account for the 0.24 eV difference in $V_{oc}$. Taken in conjunction with the lower FF of the CNC devices, this suggests that the underlying recombination dynamics and energetics of charge carriers in these systems are different.

**TABLE 1. Device Characteristics of *in Situ* and CNC Solar Cells**[a]

| | $J_{sc}$ [mA/cm$^2$] | $V_{oc}$ [mV] | FF | PCE |
|---|---|---|---|---|
| *in situ* | 7.2 | 712 | 63% | 3.2% |
| CNC | 6.7 | 475 | 48% | 1.5% |

[a] Metrics for ITO/CIS/CdS/Al solar cells.

**Bandgap and Energy Level Characterization.** To investigate differences in energetics between CNC and *in situ* CIS films, we employed ultraviolet photoelectron spectroscopy (UPS). Ionization energies (IE) of (4.9 ± 0.1) eV and (5.2 ± 0.1) eV were measured for the CNC and *in situ* CIS films, respectively, and are shown in Figure 2. CdS thin films were found to have an IE of 6.7 eV. Since CNC CIS films showed a 0.3 eV lower ionization potential than that of the *in situ* films, the offset between the conduction band of CdS and the valence band of the CIS reduces to 0.6 eV for CNC, compared to 0.9 eV for the *in situ* material. This difference accounts for the 0.24 V lower $V_{oc}$ observed for the CNC devices.

To understand the origin of this change, we note that shifts in valence band energy due to quantum confinement can be ruled out here, as these crystals are significantly larger than the Bohr radius of CIS, which is about 4.1 nm.[35] A reduction in bandgap of $CuInS_2$ nanocrystals has been previously attributed to subgap states arising from surface defects.[36] Li et al. argued that nonradiative decay occurs through surface defects in NCs.[32] However, they found that passivation of these surface states via ligands does not lead to a sharper absorption onset, suggesting that these surface defects are not responsible for the smaller bandgap and lower IE. Radiative decay in that work was posited to occur through an internal defect derived from switching of the In and Cu metal ion positions.[32] Goossens et al. argued that Cu(I) in an In(III) position can result in subgap states 0.2−0.24 eV above the valence band.[37] These emissive defects were found to be intrinsic to both CIS nanoparticles and thin films.[38] Substitutions of In with Cu atoms are typically produced under anion-deficient conditions.[39] However,

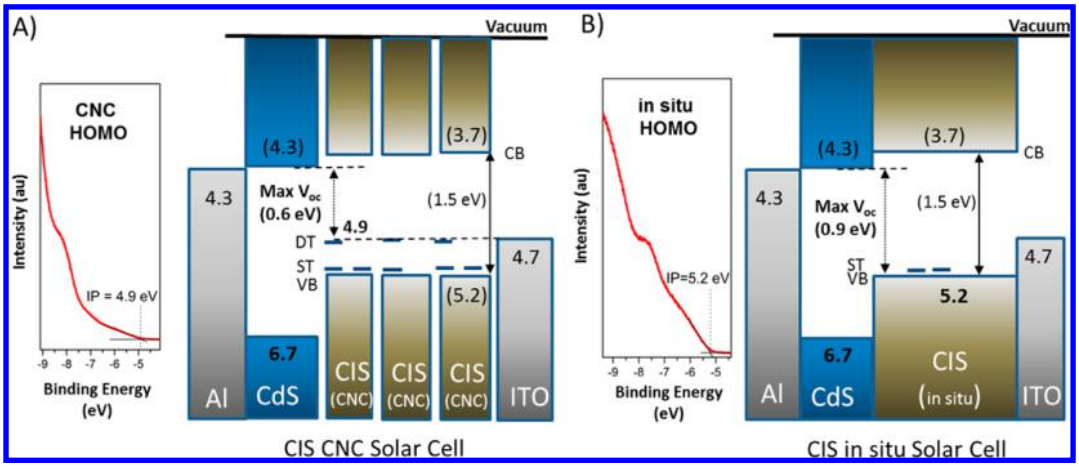


**Figure 2. Energy levels of the effective band edge states of the CIS and CdS active layers, as well as the relative energy levels of shallow hole traps (ST) and deep hole traps (DT) in the CIS films for (A) CNC and (B) *in situ* solar cells, as measured by UV photoelectron spectroscopy (UPS). The highest occupied states, as measured by UPS, for the CNC film were found to be 0.3 eV higher in energy than the valence band of the *in situ* NC film. This lowers the maximum achievable $V_{oc}$ and is attributed to the presence of deep trap (DT) states. Standard work functions of the electrodes are included for reference along with nominal conduction bands calculated using the optical band gap of each material.**

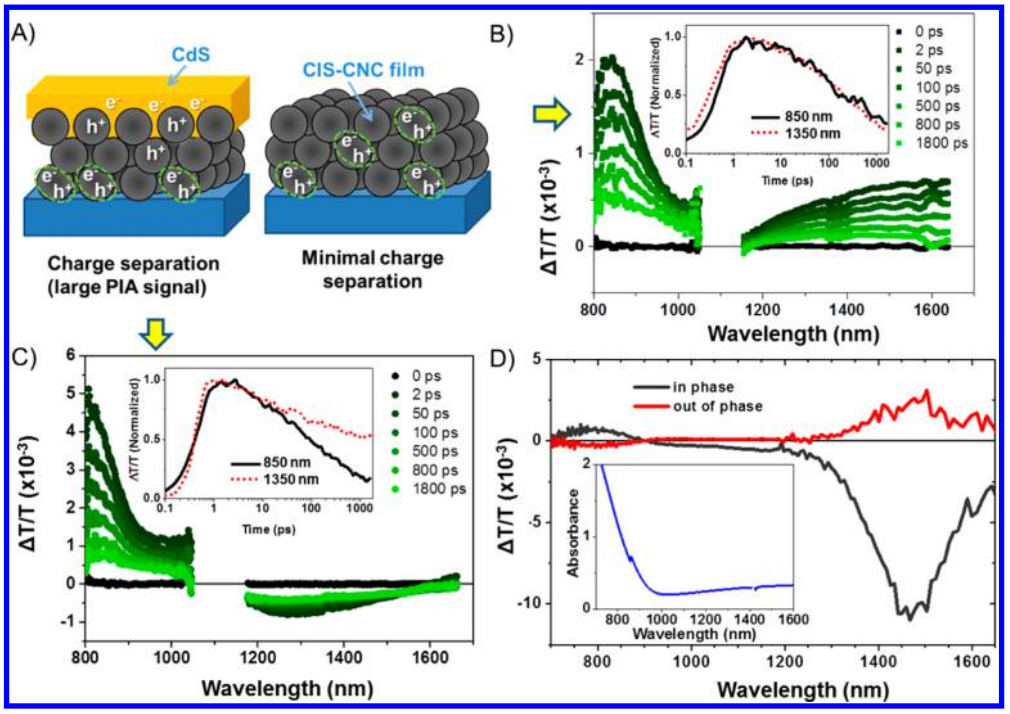


**Figure 3. (A) Simplified diagram of the CIS CNC films with (right) and without (left) CdS as an electron acceptor on quartz substrates used for ultrafast transient absorption measurements. (B) Ultrafast transient absorption measurements of CIS-CNC films on quartz showing decay of the ground-state bleach at ~850 nm and bleaching in the infrared at 1350 nm. The time decay of the GSB matches that of the infrared bleach (inset). (C) Ultrafast transient absorption measurements of CIS-CNC/CdS coated films on quartz. The decay of the GSB (inset) is faster than that of the uncoated CIS films, and a long-lived photo induced absorption has appeared in the infrared. (D) Field-modulated electroabsorption spectrum of thin films and static absorption spectrum (inset) of CNC in solution. Electroabsorption spectrum for the device (ITO/CIS-CNC/Au) was measured at 0 V dc with a modulation frequency and amplitude of 2113 Hz and 1 V, respectively, to inject holes into the CIS layer; *J*−*V* characteristics of the hole-only device can be found in the Supporting Information.**

X-ray photoelectron spectroscopy (XPS) measurements of CNC films found them instead to be Cu-deficient, compared to both the In and S content (Supporting Information), and no photoluminescence could be observed. This suggests that a copper substitutional defect is not responsible for the lower bandgap or the IE potential change in the CNC films.

Instead, the decrease in bandgap is due to an increase in copper vacancies, one of the most common defects in $CuInS_2$. These defects states have been previously found to lie ~0.10−0.15 eV above the valence band.[38] The change in IE potential, however, is most likely due to deep traps on the surface of the nanocrystals. This suggests a much larger population of deep trap sites in the CNC than in the *in situ* films. Impurities in the *in situ* film may also play a role in surface passivation, in that a large population of deep traps were not detected in the *in situ* solar cells either from the UPS or the electrical measurements. With a band gap of 3.1 and 2.0 eV, respectively, CuI or InI, if present, could decrease the prevalence of surface traps on the *in situ* CIS nanocrystals by coating the NC surface or by filling in dangling bond sites with iodide ions, ostensibly forming In−I and Cu−I bonds at the surface. A similar effect has been observed in previous studies of PbSe and PbS nanocrystals, wherein halide anions were found to passivate surface traps.[40]

**Assignment of Spectral Features for Transient Absorption on Ultrafast Time Scales.** Transient absorption (TA) spectroscopy was used to study the charge dynamics of CIS/CdS CNC and *in situ* devices (Figure 3a). Figure 3b,c shows typical transient absorption spectra for CIS and CIS/CdS films employing CNCs, respectively. These are measured in the spectral range of 800−1650 nm using an excitation wavelength of 800 nm (~300 fs pulse width). In CIS CNC films without CdS, we observe a positive peak around 850 nm with an additional large positive feature that extends up to the detection limit of 1650 nm. The positive signal at ~850 nm (1.46 eV) overlaps with the onset of the CIS absorption and is attributed to bleaching of the first excitonic absorption, equivalent to a ground-state bleach (GSB). The positive TA signal observed in the pure CIS-NC film between 1000 and 1650 nm has previously been observed in CuS and CuSe and was attributed to the bleaching of localized surface plasmons.[41] This is consistent with the sub-bandgap absorption in the near IR region observed in steady-state absorption measurements of colloidal nanocrystals in solution (blue curve in Figure 3d, inset). While some contribution from stimulated emission from defect states is possible,[38] thin films studied here exhibited low emission yields at room temperature, below our detection limit; thus, a significant contribution from stimulated emission is unlikely.

CIS films coated with CdS showed similar GSB dynamics at 850 nm (Figure 3c). However, a negative feature caused by photoinduced absorption (PIA) can be observed in the spectral region between 1200 and 1600 nm. This feature, centered around 1300 nm in the CIS-CNC/CdS film, peaks within the instrument response of 300 fs and does not appear in the pure CIS-CNC spectrum. Since excitation at 800 nm precludes exciting the CdS film directly and energy transfer from the low bandgap CIS to the wider bandgap CdS is unfavorable, we conclude that the new PIA does not arise from excited-state absorption of excitons in the CdS phase. Instead, we ascribe this feature to the absorption due to photoinduced charges.

From these results alone, this PIA feature could be ascribed to either holes on the CIS or electrons in the CdS. To determine which is the case, we performed charge-induced absorption measurements[42,43] on CIS-CNC hole-only devices (ITO/CIS/Au), which measure the change in absorption induced by the injection of holes into the CIS by a mixed ac/dc voltage bias. A detailed description can be found in the Materials and Methods. CIS-CNC hole-only devices were found to have a strong in-phase response around 1450 nm (Figure 3d). The absorption features observed here are in the same spectral region as the PIA signal in TA measurements, with a difference in peak position of less than 100 meV. We thus attribute the PIA signal observed in TA measurements to an increase in the absorption of holes in the CIS. This also means the hole absorption lies in the same spectral region as the localized surface plasmon,[41,44] suggesting that the PIA does not arise from transitions of holes to higher excited states but instead results from an increase in plasmonic absorption. This latter effect has been observed previously in cupric chalcogenides, where plasmon absorption strength increases with increased hole density.[44] While the absorption features compared above do not match exactly, this is to be expected since the stoichiometric composition of the nanocrystals is very sensitive to both synthesis conditions and oxygen exposure. Changes in oxidation state also affect hole density, which, in turn, shifts the peak of the plasmon absorption.[44]

Having identified the additional PIA feature in the CIS/CdS blend as being due to the CIS hole plasmon, the absence of this feature in pure CIS films indicates that direct photoinduced charge generation is not efficient within the CIS phase. This suggests that CIS/CdS devices are excitonic in nature, which explains the requirement for a CIS/CdS interface to form separated charges.

The appearance of the hole plasmon PIA within the instrument response time (300 fs) indicates that diffusion of excitons in the CIS is not the dominant process in charge generation. This, and the lack of a later growth of the PIA, indicates that only excitons generated at or very near the CdS interface result in the formation of charges. The relatively high EQEs above 20% would then indicate a larger interfacial area than that of a simple planar heterojunction. This suggests that the CIS/CdS devices do not form a bilayer but that the CdS penetrates the mesoporous structure of the CIS.

The positive plasmonic bleach observed in the CNC-only films (Figure 3b) is broader and red-shifted compared to the PIA signal observed during TA measurements in CIS/CdS films, which requires some explanation. Kriegel et al. found that pulsed photoexcitation of pristine copper chalcogenide NCs resulted in a red-shifted plasmonic bleach when compared to steady-state measurements and attributed this to the heating of the carrier gas.[41] The plasmonic feature was also broader than in steady-state measurements, which was assigned to a pump-induced increase in charge carrier scattering, resulting in a damping of the plasmonic resonance. By analogy to the behavior of gold nanoparticles,[45] Kriegel et al. argued that, upon pulsed photoexcitation, scattering of charge carriers by defects and with one another, accompanied by heating of the charge carrier population, induces a broadened plasmonic bleach.[41]

We find the spectral shape of the PIA observed in CIS/CdS films to be in good agreement with the steady-state hole plasmon absorption described by Kriegel et al. Since both the PIA in CIS/CdS films and the plasmonic bleach in CIS-CNC films appear within the instrument response, and similar excitation densities are used, it is unlikely that the relative red shift and broadening of the plasmonic bleach is solely caused by an enhancement in heating and charge carrier scattering. Instead, in CIS-only films the plasmon appears red-shifted and broader, more likely due to the electronic coupling between the photoinduced electron and the positively charged surface plasmon. In this interpretation, the electron damps the resonance of the localized hole, leading to a lower absorption (positive signal) and broader spectral shape. By introducing an electron acceptor such as CdS, the photoinduced electron can be removed from the CIS. Once the electron is transferred, the plasmon oscillation is no longer damped and the photoinduced hole results in an increased plasmonic absorption (PIA signal in Figure 3c).

**Transient Photovoltage and Photocurrent Measurements.** To understand how the behavior of charges separated at the CIS/CdS interface differs between the device types, we conducted time-resolved photocurrent and photovoltage measurements. For transient photocurrent (TPC), a light pulse is applied to a device held at short circuit under white-light bias (WLB), and the resulting photocurrent measured over time. From this, we measure the time it takes to extract photogenerated charges, defining the extraction lifetime $\tau_e$ as the time taken for the current to drop to 1/e of its initial

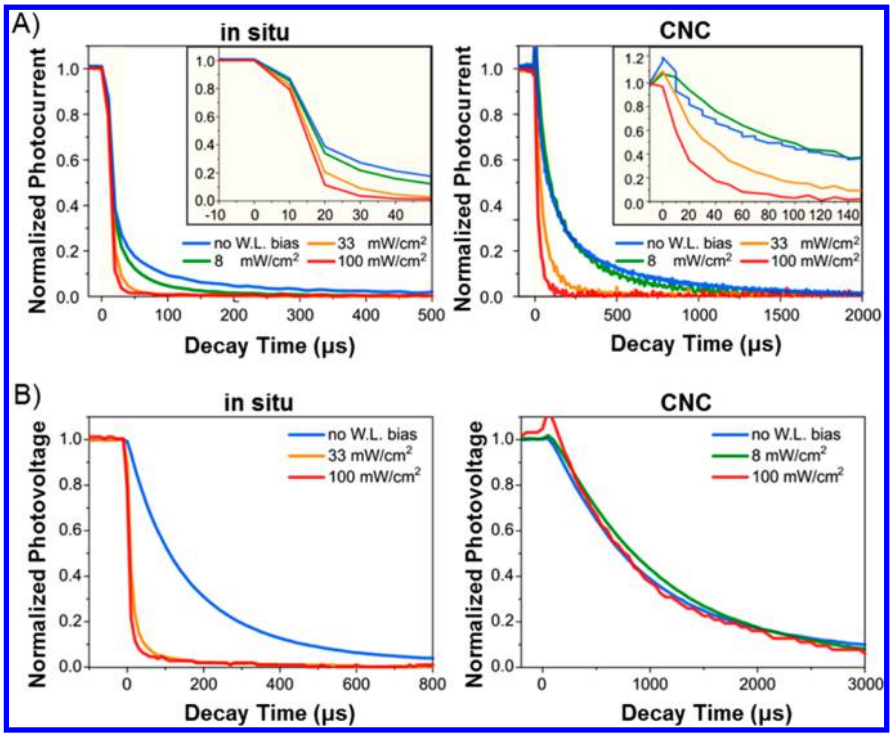


**Figure 4. Transient photocurrent (A) and photovoltage (B) decay as a function of white-light bias. The normalized initial decay in transient photocurrent is shown in the inset.**

steady-state value. TPC measurements as a function of a WLB are shown in Figure 4a along with the respective TPC lifetimes $\tau_e$ in Table 2. The majority of the charges in the *in situ* devices underwent fast extraction on the order of ~20 $\mu$s. We also observed a photocurrent tail extracted on time scales of hundreds of microseconds, which we interpret as charges thermally released from deep traps. With increasing WLB, extraction times decrease and the long-lived tail disappears, suggesting that such traps become filled at higher excitation densities. To quantify the contribution to the photocurrent from the detrapping of long-lived trapped charges, we define short- and long-lived charges as those extracted before or after $\tau_e$, respectively, and fit the long-lived tail of the transient photocurrent decay using an exponential function extrapolated to time zero. In all cases, contribution from trapped charge decreases with increasing WLB. The decrease in extraction time and the suppression of the long-lived photocurrent tail is consistent with the presence of a low density of shallow traps. By increasing the WLB, these traps may be filled by photogenerated carriers, increasing the average mobility of the charge carrier population and thus facilitating charge extraction. Charges generated by the transient light pulse are thus less likely to become trapped themselves, reducing the relative contribution of trapped charges to the photocurrent.

For *in situ* CIS/CdS devices with no WLB, ~7% of the photocurrent was found to arise from charges that are initially trapped. At a WLB of 100 mW/cm$^2$, their contribution drops below ~2%. CNC devices exhibited

**TABLE 2. Transient Photocurrent Decay Constants of *in Situ* and CNC CIS Devices under Different Background Illuminations[a]**

| | no WLB | 8 mW/cm$^2$ | 33 mW/cm$^2$ | 100 mW/cm$^2$ |
|---|---|---|---|---|
| $\tau_e$ (*in situ*) [$\mu$s] | 22 | 19 | 17 | 16 |
| $\tau_e$ (CNC) [$\mu$s] | 140 | 154 | 48 | 19 |

[a] TPC decay times for ITO/CIS/CdS/Al solar cells under white-light bias (WLB).

a much stronger effect of white-light bias on both extraction times and the amount of trapped charge. Without WLB, 40% of the photocurrent originates from charges trapped at very early times after excitation. At 100 mW/cm$^2$ WLB, the photocurrent contribution of these trapped charges, most of which were extracted within ~200 $\mu$s, was reduced to about 10−15%. The large contribution of trap states to photocurrent even at higher WLB suggests the presence of a large trap density in the CNC devices, most likely related to surface defects.[32]

It is important to note that absolute TPC lifetimes are dependent on the hopping rates between neighboring NCs, which depend strongly on the nature of the tunnelling barriers between them. CNCs can be expected to exhibit nearest and next-nearest neighbor hopping conduction,[46−48] whereas conduction in the semi-sintered *in situ* films probably benefits from a mix of hopping and band-like transport. This is reflected in the generally faster TPC decay rates of the *in situ* films. Under varying white-light biases, it is the change in the decay rate that indicates the degree of trapping in the

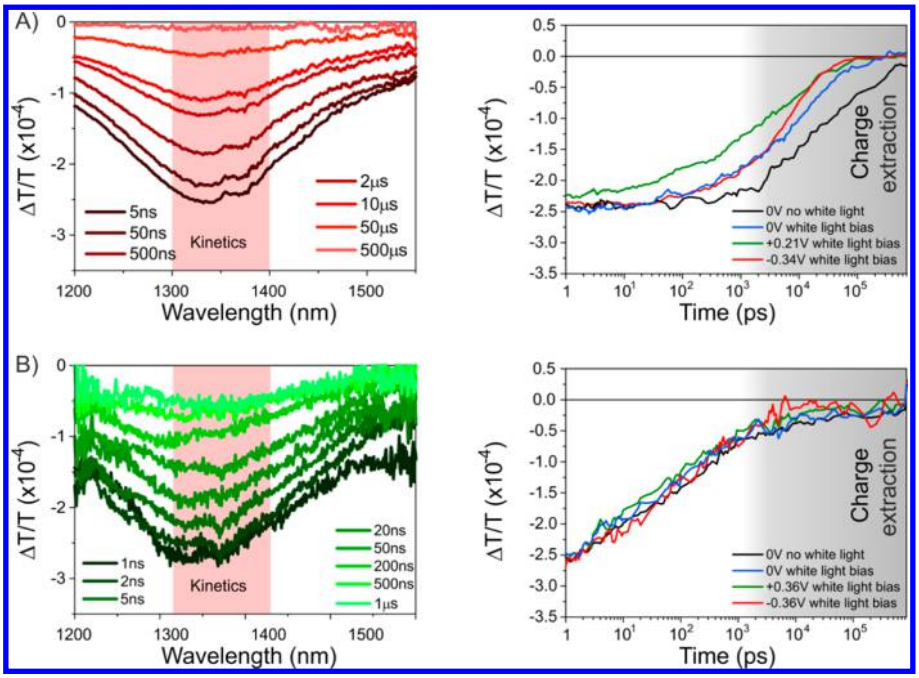


**Figure 5. Spectrally resolved long-time IR transient absorption measurements (left) with the PIA signal (right) integrated between 1350 and 1450 nm for the (A) CIS *in situ* and (B) CIS CNC solar cells.**

film as photogenerated charges fill traps and increase the overall carrier concentration. The fact that the decay rates are relatively unchanged in the *in situ* film under WLB suggests that defects and impurities, such as CuI, InI, and remaining ligands, do not play a strong role in charge trapping and may, in fact, suppress this effect. The average distance between NCs is in this experiment is unchanged, and, given similar absorbance profiles, EQEs, $J_{SC}$, and dimensions, the photogenerated carrier concentration is likely to be similar as well. Thus, the difference in the TPC decay between the WLB and zero WLB cases in Figure 4 is mainly due to the degree to which trap filling is responsible for the change in the TPC decay rates.

In contrast to TPC, transient photovoltage (TPV) decay measures the change in voltage induced by a light pulse and thus gives insight into the internal recombination dynamics of the charge carriers, since no external current flows. Figure 4b (left panel) shows the photovoltage decay time for *in situ* devices at different white-light biases. In the absence of WLB, a TPV lifetime of ~150 $\mu$s was measured. At a WLB of nearly 100 mW/cm$^2$, the TPV lifetime drops to 15 $\mu$s. Nearly 95% of the population was found to decay via this fast channel.

TPV lifetimes for CNC devices were largely independent of white-light bias and were longer-lived, with lifetimes of ~1000 $\mu$s for WLBs between 0 and 100 mW/cm$^2$ (Figure 4b, right panel). Since the CdS treatment was the same for the *in situ* and CNC devices, it is unlikely that the CdS layer is responsible for the reduction in charge recombination. The similar TPV decay time at 0 and 100 mW/cm$^2$ WLB indicates that charge recombination within this intensity range does not depend on trap filling. In combination with the long decay times under zero WLB, this indicates that holes are deeply trapped in the CNC CIS film over long periods of time.

**Long-Time Transient Absorption on Solar Cells.** In functional solar cells, charges can undergo trapping and nongeminate recombination processes or be transported to and extracted at the electrode. The observation of a hole-induced PIA signal gives us the ability to trace the kinetics of these charges directly. Figure 5 shows the time evolution of the hole PIA signal between 1350 and 1450 nm for functioning CIS/CdS cells in forward, reverse, and at zero voltage bias. The *in situ* and CNC devices in Figures 5 were measured under low intensity (~10 mW/cm$^2$) and zero WLB, for comparison.

In the *in situ* solar cell (Figure 5a), we observed a relatively long-lived hole signal for all biases. Devices measured at short circuit and without white-light bias showed the longest charge lifetime, decaying to 1/e of the initial PIA amplitude within 45 $\mu$s. With low-intensity WLB, this lifetime is reduced to 12 $\mu$s at short circuit, 8 $\mu$s at −0.34 V reverse bias, and 5 $\mu$s at +0.21 V forward bias. From these lifetimes, we conclude that carrier extraction occurs on microsecond time scales. This is in good agreement with photocurrent decay times obtained from TPC measurements, whereas the dependence of extraction time on WLB indicates some carrier trapping, also consistent with the TPC measurements. Devices measured with WLB also showed a faster decay in hole PIA at times <1 $\mu$s. We attribute this to an increase in nongeminate recombination, since the white light increases the charge density in the device. In forward bias, the early time decay is faster

still, which we attribute to increased nongeminate recombination arising both from the higher charge densities at forward bias and the reduced physical separation of electrons and holes as the internal field drops.

The CNC solar cells exhibited a much faster decay of the PIA signal, with a half-life of 100 ns. In contrast to *in situ* devices, the dependence of decay time on applied voltage and white-light bias is much weaker. It is also notable that at short circuit the signal does not decay fully but plateaus at around 10 $\mu$s. At reverse bias of −0.36 V, this plateau is reduced. The TA signal of the CNC devices decays much faster than expected from the TPC, from which we expect extraction to occur at similar or longer time scales than those in the *in situ* devices and to start from about 1 $\mu$s. However, on time scales when charge extraction is observed in the TPC measurements, TA measurements reveal a large fraction of the hole PIA to have decayed. At 1 $\mu$s, only 25% of the original TA signal in CNC devices remains. If this signal were to represent extractable charge, then this result would be in conflict with the IV and EQE characteristics of these devices and is not consistent with the hole kinetics measured in *in situ* devices.

Instead, we conclude that the TA signal at 1400 nm is not measuring the entire population of holes in the film but, rather, the fraction of mobile holes that enhance the surface plamon absorption, thus contributing to PIA. Interpreted this way, the initial decay in TA signal between 1 ns and 1 $\mu$s in CNC devices is due to deep trapping of free holes. Once a hole becomes localized to a deep trap, it does not support plasmonic oscillation, resulting in a decay of the negative TA feature at 1400 nm. Since the *in situ* devices show no significant decay within the first microsecond, we conclude that deep trapping in these devices is less prevalent. This is also consistent with our TPC measurements, where CNC devices exhibited slower extraction kinetics than *in situ* devices, suggesting a larger degree of trapping. The long-lived TA contribution in CNC films ($t$ > 100 $\mu$s) can thus be attributed to detrapping holes, which are again detectable via the characteristic enhanced plasmon absorption around 1400 nm.

## CONCLUSIONS

In summary, we have probed the charge dynamics in CIS devices using transient photocurrent, transient photovoltage, and transient absorption techniques. Charge extraction and recombination kinetics in colloidal nanocrystals (CNC) were found to exhibit a much stronger dependence on the background white-light bias than that of *in situ* devices, suggesting a larger trap density in CNC CIS. While no charge signal was observed in CIS-only films, transient absorption measurements conducted on CIS/CdS films revealed an instrument-response-limited hole generation. This suggests that these devices are excitonic in nature and require the CdS interface to separate charges. Long-time transient absorption measurements of *in situ* devices were found to be in good agreement with their TPC/TPV measurements. While *in situ* devices showed no significant decay of the hole plasmon within the first microsecond, hole-plasmon induced PIA signals in CNC devices were found to decay by 75% in the same time period, much faster than anticipated from TPC measurements. We thus conclude that the observed fast decay in hole-plasmon induced PIA in CNC devices is due to deep trapping of free holes, resulting in a decrease in plasmonic absorption. These results indicate that charge dynamics in CNC devices are dominated by deep traps, most likely from surface defects on the nanocrystals. Better control of the nanocrystal surface and nanocrystal chemistry is thus essential for improving device performance. Ultimately, better understanding of the physics of cupric chalcogenide nanocrystal devices should lead to nanocrystal solar cells that can better deliver on the promise of cheap and scalable solar power.

## MATERIALS AND METHODS

**CIS Colloidal Nanocrystals (CIS CNC).** In a typical synthesis of CIS nanocrystals, 1 mmol of copper(I) iodide, 1 mmol of indium acetate hydrate, and 1 mmol of thiourea were added to 12 mL of oleylamine. The mixture was degassed under vacuum at 100 °C and then heated at 180 °C for 1 h before cooling quickly to room temperature. Nanocrystals were purified under nitrogen using standard solvent/nonsolvent purification methods in an inert atmosphere using isopropanol and methanol/butanol as the nonsolvents and hexane as a solvent. After two to three repeated purification steps, the resulting aggregated materials were redispersed in anhydrous chloroform and filtered through a 0.45 $\mu$m PTFE syringe filter to form a 20 mg/mL stock solution. Transmission electron microscope images revealed samples of large, nonuniform spheroidal nanocrystals with principle dimensions of (10 ± 3) nm in width, as measured on the longest apparent axial dimension (see Supporting Information). X-ray diffraction (XRD) spectra of the nanocyrstals correspond well with the wurtzite crystal structure.[49,50] Although samples with superior monodispersity could be achieved using 1-dodecanethiol or oleylamine-sulfur precursors, thick films of such NCs were found to be very resistive and were not found to make efficient solar cells.

**CIS CNC Thin Film Preparation.** Thick films of CIS CNCs were formed using the layer-by-layer (LBL) technique via spin coating. In brief, nanocrystals were deposited onto a cleaned, patterned, conductive ITO/glass substrate by spin coating a stock solution in chloroform at 2000 rpm for 1 min in an inert atmosphere. A solution of 0.2% 1,3-benzenedithiol (BDT) in acetonitrile, a cross-linking agent to replace the native ligands groups, was then drop cast onto the substrate and left for 10 s prior to spin casting, again at 2000 rpm for 1 min. This step was repeated with pure acetonitrile to remove excess cross-linking agent. These three steps were repeated an arbitrary number of times to achieve films with an optical density of ∼0.50 at 500 nm. This thickness was comparable in absorbance to CIS *in situ* devices reported previously and permitted nearly complete absorbance of solar light in the device while still permitting spectroscopic examination with near-IR and visible

wavelengths. It should be noted that LBL techniques do not necessarily replace all of the native capping groups; however, they can be clearly observed to change the solubility of the CNCs already deposited, preventing redispersal of previous films and generally increasing the conductivity.

**CIS *in Situ* Thin Film Preparation.** Thin films of CIS *in situ* nanocrystals were formed using a method adapted from Li et al.[18] wherein 90 mg of copper(I) iodide, 120 mg of indium(III) acetate, and 150 mg of thiourea were dissolved in a solution of 2.4 mL of *n*-butylamine and 0.16 mL of propionic acid. This solution was mixed just prior to spin coating in an inert atmosphere. Thin films were spin-coated onto cleaned, patterned, conductive ITO/glass substates at 1500 rpm and heated at 250 °C for 10 min prior to CdS coating. The *in situ* nanocrystals appeared to be weakly crystalline, although they nominally correspond to the chalcopyrite crystal structure, as determined by XRD.[49,50] It is also noted that the sol−gel synthesis can leave iodide impurities in the film, although these are greatly reduced after the second CdS deposition step to ∼2% (see Supporting Information for further discussion of the role of impurities).

**CdS Thin Film Preparation.** Thin films of cadmium sulfide were formed on the CIS absorber layers using a method adapted from Li et al.[18] wherein 70 mg of cadmium chloride and 190 mg of thiourea were dissolved in a solution of 4 mL of *n*-butylamine and 0.16 mL of propionic acid. This solution was mixed just prior to spin coating in an inert atmosphere. Thin films were spin-coat onto ITO/glass substrates coated with CNC or *in situ* formed CIS at 1500 rpm and heated at 250 °C for 10 min prior to cooling to room temperature.

Device fabrication: Prepatterned ITO/glass substrates were cleaned by sonication in acetone and isopropanol prior to spin coating thin films of *in situ* CIS or layer-by-layer films of CIS CNCs. Films were then spin-coated with a CdS layer of ∼50 nm. Aluminum electrodes of 100 nm thickness were evaporated through a shadow mask onto the CdS layer to form the reflective top electrode. All device processing and subsequent packing were performed in a nitrogen glovebox.

**Materials Characterization.** *Transmission Electron Microscopy.* TEM was performed using a FEI Philips Tecnai 20 on nanocrystals deposited from chloroform onto carbon-coated copper grids (Ted Pella). Statistics were collected by measuring the length of the major axis for over 100 nanocrystals.

*Thin Films Material Characterization.* XRD was performed on dried powder CNCs and *in situ* films using a PANAlyticalX'Pert Pro XRD system with Cu Kα radiation ($\lambda$ = 0.1541 nm) and a position-sensitive detector. SEM and EDS on cleaved devices and thin films were performed using a Hitachi S-5500 in-lens FE SEM. Surface and composition of the *in situ* and CNC thin films (see Supporting Information) were investigated using a JEOL 6610LV SEM.

*Photoemission Spectroscopy.* XPS and UPS were performed using a Thermo Scientific Escalab 250Xi XPS/UPS system on thin films deposited onto p-type conductive silicon substrates using the methods described above. In UPS, the low-energy edge of the valence band was used to determine the ionization potential of the thin film.[51,52]

*Absorbance Measurements.* Films were spin-cast on ITO/glass substrates, and the spectra were collected using an HP 8453 UV−vis spectrometer. CNC solution spectroscopy was performed on the CIS stock solution using a PerkinElmer Lambda 9 UV−vis−IR spectrometer.

**Device Characterization.** *Power Conversion Efficiency.* PCE was measured using a Keithley 2636A source measure unit and an Oriel 92250A solar simulator. Solar output was adjusted to a calibrated reference, and device measurements were then corrected for spectral mismatch to the reference.

*External Quantum Efficiency.* EQE was measured as a function of photon wavelength. Monochromatic light was obtained using xenon lamp light passed through an Oriel Cornerstone 260 monochromator. EQEs were calculated in comparison to the response from a calibrated reference diode.

*Transient Photocurrent (TPC) and Photovoltage (TPV).* Transient photocurrent and photovoltage were performed using 525 nm green LED (Kingbright, L-7104VGC-H) connected to an HP 8116A pulse/function generator producing a square voltage pulse. Pulse power of the light from the diode, while on, was approximately 5 mW/cm$^2$ at the target, with a pulse width of 2 to 5 ms (to achieve steady-state dynamics prior to shutoff). Current response was measured by connecting an Agilent DSO6052A digitizing oscilloscope in series with an input impedance of 50 Ω. The voltage response from the solar cell was recorded using the same oscilloscope connected in series with a 1 MΩ impedance. Measurements were taken with and without background white-light bias of up to ∼1 sun intensity as measured against a calibrated reference cell.

*Short-Time Transient Absorption Spectroscopy.* For ultrafast TA spectroscopy, the output of a 1 kHz regenerative amplifier (Spectra-Physics Solstice) was used to seed a traveling optical parametric amplifier (TOPAS) (Light Conversion), generating a narrowband (20 nm) pulse (pulse length of 100−300 fs) that served as the excitation source. The transmission of the sample was probed before ($T_0$) and after excitation ($T_1$), using the broadband (850−1050 nm) output of a home-built non-collinear optical parametric amplifier (NOPA). The transient absorption signal $\Delta T/T$ is then obtained by $\Delta T/T = (T_1 - T_0)/T_0$.

To reduce the noise induced by laser fluctuations, the probe beam was split to provide a reference signal, which was used to account for shot to shot variations. Both probe and reference beams were coupled into a Andor Shamrock SR-303i spectrometer and detected using a pair of 16-bit 1024-pixel linear image sensors (Hamamatsu, S8381-1024Q), which were driven and read out at 1 kHz by a custom-built board from Stresing Entwicklunsbuero.

*Long-Time Transient Absorption Spectroscopy.* Pump pulses for long-time experiments (1 ns < $t$ < 1 ms) were generated by a frequency-doubled Q-switched Nd:YVO4 laser (AOT-YVO-25QSPX, Advanced Optical Technologies), with a pulse length of ∼600 ps. The probe and pump pulses were synchronized using a Stanford Research Systems (SRSDG535) electronic delay generator, which allowed TA signals to be measured between 1 ns and 1 ms. Changes in absorption were measured using the same setup as for short-time transient absorption spectroscopy measurements.

*Electroabsorption Measurements.* A tungsten lamp was used as a white-light source and connected to a Chromex SM monochromator. The monochromatic light was focused at an angle of 45° on the device through the ITO side and reflected off the gold electrode onto a Thorlabs amplified InGaAs detector. A 1 V ac bias was applied on the device using a lock-in amplifier (Stanford Research Systems SR830 DSP) at a modulation frequency 2113 Hz. To obtain the modulated absorption response, we split the output of the photodetector into a dc component $I_0T$ measured with a Keithley 2400 source meter and an ac component $I_0\Delta T$ measured with the lock-in amplifier. The oscillating signal $I_0\Delta T$ measures the change in absorption induced by the modulated voltage bias applied by lock-in, whereas the dc signal measures the steady-state absorption of the sample. The in-phase and out-of-phase $\Delta T/T$ responses are obtained by dividing the respective ac component by the dc component.

*Conflict of Interest:* The authors declare no competing financial interest.

*Supporting Information Available:* TEM, UPS, XPS, and XRD characterization of CIS colloidal nanocrystals (CNC); XPS and UPS characterization of thin films; SEM characterization of the CNC device structure including EDX analysis, ultrafast transient absorption on functional devices prior to operation, optical spectra of CNC CIS nanoparticles in solution, and absorption spectra of both CNC and *in situ* films on ITO glass; EDS, XRD, and SEM analysis of all the thin films used; and impurity analysis and discussion. The Supporting Information is available free of charge on the ACS Publications website at DOI: 10.1021/acsnano.5b00432. Data supporting this publication are available at http://www.repository.cam.ac.uk/handle/1810/247778.

*Acknowledgment.* We gratefully acknowledge support by EPSRC (grant no. EP/G060738/1), Cambridge Display Technology, and the Worshipful Company of Armourers & Brasiers for a Gauntlet Trust award, as well as the MacDiarmid Institute for use of their EM facilities. We thank Iyad Nasrallah for useful discussions and experimental assistance.

## REFERENCES AND NOTES


1. Todorov, T. K.; Gunawan, O.; Gokmen, T.; Mitzi, D. B. Solution-Processed Cu(In,Ga)(S,Se)$_2$ Absorber Yielding a 15.2% Efficient Solar Cell. *Prog. Photovoltaics* **2013**, *21*, 82–87.
2. Liu, W.; Mitzi, D. B.; Yuan, M.; Kellock, A. J.; Chey, S. J.; Gunawan, O. 12% Efficiency CuIn(Se,S)$_2$ Photovoltaic Device Prepared Using a Hydrazine Solution Process. *Chem. Mater.* **2010**, *22*, 1010–1014.
3. Bag, S.; Gunawan, O.; Gokmen, T.; Zhu, Y.; Mitzi, D. B. Hydrazine-Processed Ge-Substituted CZTSe Solar Cells. *Chem. Mater.* **2012**, *24*, 4588–4593.
4. Gunawan, O.; Todorov, T. K.; Mitzi, D. B. Loss Mechanisms in Hydrazine-Processed $Cu_2ZnSn(Se,S)_4$ Solar Cells. *Appl. Phys. Lett.* **2010**, *97*, 233506.
5. Ning, Z.; Zhitomirsky, D.; Adinolf, V.; Sutherland, B.; Xu, J.; Voznyy, O.; Maraghechi, P.; Lan, X.; Hoogland, S.; Ren, Y.; Sargent, E. H. Graded Doping for Enhanced Colloidal Quantum Dot Photovoltaics. *Adv. Mater.* **2013**, *25*, 1719–1723.
6. Cho, A.; Ahn, S.; Yun, J. H.; Gwak, J.; Song, H.; Yoon, K. A Hybrid Ink of Binary Copper Sulfide Nanoparticles and Indium Precursor Solution for a Dense $CuInSe_2$ Absorber Thin Film and Its Photovoltaic Performance. *J. Mater. Chem.* **2012**, *22*, 17893–17899.
7. Cao, Y.; Denny, M. S., Jr.; Caspar, J. V.; Farneth, W. E.; Guo, Q.; Ionkin, A. S.; Johnson, L. K.; Lu, M.; Malajovich, I.; Radu, D.; Rosenfeld, H. D.; Choudhury, K. R.; Wu, W. High-Efficiency Solution-Processed $Cu_2ZnSn(S,Se)_4$ Thin-Film Solar Cells Prepared from Binary and Ternary Nanoparticles. *J. Am. Chem. Soc.* **2012**, *134*, 15644–15647.
8. Akhavan, V. A.; Goodfellow, B. W.; Panthani, M. G.; Steinhagen, C.; Harvey, T. B.; Stolle, C. J.; Korgel, B. A. Colloidal CIGS and CZTS Nanocrystals: A Precursor Route to Printed Photovoltaics. *J. Solid State Chem.* **2012**, *189*, 2–12.
9. Tang, J.; Sargent, E. H. Infrared Colloidal Quantum Dots for Photovoltaics: Fundamentals and Recent Progress. *Adv. Mater.* **2011**, *23*, 12–39.
10. Khare, A.; Wills, A. W.; Ammerman, L. M.; Norris, D. J.; Aydil, E. S. Size Control and Quantum Confinement in $Cu_2ZnSnS_4$ Nanocrystals. *Chem. Commun.* **2011**, *47*, 11721–11723.
11. Wang, J.-J.; Wang, Y.-Q.; Cao, F.-F.; Guo, Y.-G.; Wan, L.-J. Synthesis of Monodispersed Wurtzite Structure $CuInSe_2$ Nanocrystals and Their Application in High-Performance Organic–Inorganic Hybrid Photodetectors. *J. Am. Chem. Soc.* **2010**, *132*, 12218–12221.
12. Talapin, D.; Lee, J.-S.; Kovalenko, M. V.; Shevchenko, E. V. Prospects of Colloidal Nanocrystals for Electronic and Optoelectronic Applications. *Chem. Rev.* **2010**, *110*, 389–458.
13. Liu, C.-Y.; Kortshagen, U. R. A Silicon Nanocrystal Schottky Junction Solar Cell Produced From Colloidal Silicon Nanocrystals. *Nano. Res. Lett.* **2010**, *5*, 1253–1256.
14. Konstantatos, G.; Sargent, E. H. Nanostructured Materials for Photon Detection. *Nat. Nanotechnol.* **2010**, *5*, 391–400.
15. Habas, S. E.; Platt, H. A. S.; van Hest, M. F. A. M.; Ginley, D. S. Low-Cost Inorganic Solar Cells: From Ink to Printed Device. *Chem. Rev.* **2010**, *110*, 6571–6594.
16. Guo, Q.; Ford, G. M.; Yang, W.-C.; Walker, B. C.; Stach, E. A.; Hillhouse, H. W.; Agrawa, R. Fabrication of 7.2% Efficient CZTSSe Solar Cells Using CZTS Nanocrystals. *J. Am. Chem. Soc.* **2010**, *132*, 17384–17386.
17. Steinhagen, C.; Panthani, M. G.; Akhavan, V.; Goodfellow, B.; Koo, B.; Korgel, B. A. Synthesis of $Cu_2ZnSnS_4$ Nanocrystals for Use in Low-Cost Photovoltaics. *J. Am. Chem. Soc.* **2009**, *131*, 12554–12555.
18. Li, L.; Coates, N.; Moses, D. Solution-Processed Inorganic Solar Cell Based on *in Situ* Synthesis and Film Deposition of $CuInS_2$ Nanocrystals. *J. Am. Chem. Soc.* **2009**, *132*, 22–23.
19. Hillhouse, H. W.; Beard, M. C. Solar Cells from Colloidal Nanocrystals: Fundamentals, Materials, Devices, and Economics. *Curr. Op. Col. Inter. Sci.* **2009**, *14*, 245–259.
20. Guo, Q.; Hillhouse, H. W.; Agrawal, R. Synthesis of $Cu_2ZnSnS_4$ Nanocrystal Ink and Its Use for Solar Cells. *J. Am. Chem. Soc.* **2009**, *131*, 11672–11673.
21. Arango, A. C.; Oertel, D. C.; Xu, Y.; Bawendi, M. G.; Bulović, V. Heterojunction photovoltaics using printed colloidal quantum dots as a photosensitive layer. *Nano Lett.* **2009**, *9*, 860–863.
22. Panthani, M. G.; Akhavan, V.; Goodfellow, B.; Schmidtke, J. P.; Dunn, L.; Dodabalapur, A.; Barbara, P. F.; Korgel, B. A. Synthesis of $CuInS_2$, $CuInSe_2$, and $Cu(In_xGa_{1-x})Se_2$ (CIGS) Nanocrystal "Inks" for Printable Photovoltaics. *J. Am. Chem. Soc.* **2008**, *130*, 16770–16777.
23. Luther, J. M.; Law, M.; Beard, M. C.; Song, Q.; Reese, M. O.; Ellingson, R. J.; Nozik, A. J. Schottky Solar Cells Based on Colloidal Nanocrystal Films. *Nano Lett.* **2008**, *8*, 3488–3492.
24. Koleilat, G. I.; Levina, L.; Shukla, H.; Myrskog, S. H.; Hinds, S.; Pattantyus-Abraham, A. G.; Sargent, E. H. Efficient, Stable Infrared Photovoltaics Based on Solution-Cast Colloidal Quantum Dots. *ACS Nano* **2008**, *2*, 833–840.
25. Kamat, P. V. Quantum Dot Solar Cells: Semiconductor Nanocrystals as Light Harvesters. *J. Phys. Chem. C* **2008**, *112*, 18737–18753.
26. Goossens, A.; Hofhuis, J. Spray-Deposited $CuInS_2$ Solar Cells. *Nanotechnology* **2008**, *19*, 424018.
27. Tanaka, K.; Moritake, N.; Uchiki, H. Preparation of $Cu_2ZnSnS_4$ Thin Films by Sulfurizing Sol-Gel Deposited Precursors. *Sol. Energy Mater. Sol. Cells* **2007**, *91*, 1199–1201.
28. Willis, S. M.; Cheng, C.; Assender, H. E.; Watt, A. A. R. The Transitional Heterojunction Behavior of PbS/ZnO Colloidal Quantum Dot Solar Cells. *Nano Lett.* **2012**, *12*, 1522–1526.
29. Ehrler, B.; Walker, B. J.; Böhm, M. L.; Wilson, M. W. B.; Vaynzof, Y.; Friend, R. H.; Greenham, N. C. *In situ* Measurement of Exciton Energy in Hybrid Singlet-Fission Solar Cells. *Nat. Commun.* **2012**, *3*, 1019.
30. Tang, J.; Sargent, E. H. Infrared Colloidal Quantum Dots for Photovoltaics: Fundamentals and Recent Progress. *Adv. Mater.* **2011**, *23*, 12–29.
31. Zhao, N.; Osedach, T. P.; Chang, L.-Y.; Geyer, S. M.; Wanger, D.; Binda, M. T.; Arango, A. C.; Bawendi, M. G.; Bulovic, V. Colloidal PbS Quantum Dot Solar Cells with High Fill Factor. *ACS Nano* **2010**, *4*, 3743–3752.
32. Li, L.; Pandey, A.; Werder, D. J.; Khanal, B. P.; Pietryga, J. M.; Klimov, V. I. Efficient Synthesis of Highly Luminescent Copper Indium Sulfide-Based Core/Shell Nanocrystals with Surprisingly Long-Lived Emission. *J. Am. Chem. Soc.* **2011**, *133*, 1176–1179.
33. Xie, R.; Rutherford, M.; Peng, X. Formation of High-Quality I-III-VI Semiconductor Nanocrystals by Tuning Relative Reactivity of Cationic Precursors. *J. Am. Chem. Soc.* **2009**, *131*, 5691–5697.
34. Mulder, B. J. Optical Properties and Energy Band Scheme of Cuprous Sulphides with Ordered and Disordered Copper Ions. *Phys. Status Solidi A* **1973**, *18*, 633.
35. Kolny-Olesiak, J.; Weller, H. Synthesis and Application of Colloidal $CuInS_2$ Semiconductor Nanocrystals. *ACS Appl. Mater. Interfaces* **2013**, *5*, 12221–37.
36. Castro, S. L.; Bailey, S. G.; Raffaelle, R. P.; Banger, K. K.; Hepp, A. F. Nanocrystalline Chalcopyrite Materials($CuInS_2$ and $CuInSe_2$) via Low-Temperature Pyrolysis of Molecular Single-Source Precursors. *Chem. Mater.* **2003**, *15*, 3142–32147.
37. Goossens, A.; Hofhuis, J. Spray-Deposited $CuInS_2$ Solar Cells. *Nanotechnology* **2008**, *19*, 424018.
38. Castro, S. L.; Bailey, S. G.; Raffaelle, R. P.; Banger, K. K.; Hepp, A. F. Synthesis and Characterization of Colloidal $CuInS_2$ Nanoparticles from a Molecular Single-Source Precursor. *J. Phys. Chem. B* **2004**, *108*, 12429–12435.
39. Hishida, Y.; Toda, T.; Yoshie, T.; Yagi, K.; Yamaguchi, T.; Niina, T. Suppression of Cu Diffusion from a Bulk ZnSe Substrate to a Homoepitaxial Layer by Se Beam Irradiation as a Pregrowth Treatment. *Appl. Phys. Lett.* **1994**, *64*, 3419–3421.
40. Zhang, J.; Gao, J.; Miller, E. M.; Luther, J. M.; Beard, M. C. Diffusion-Controlled Synthesis of PbS and PbSe Quantum Dots with *in-situ* Halide Passivation for Quantum Dot Solar Cells. *ACS Nano* **2014**, *8*, 614–622.

41. Kriegel, I.; Jiang, C.; Rodriguez-Fernandez, J.; Schaller, R. D.; Talapin, D. V.; da Como, E.; Feldmann, J. Tuning the Excitonic and Plasmonic Properties of Copper Chalcogenide Nanocrystals. *J. Am. Chem. Soc.* **2012**, *134*, 1583–90.
42. Brown, T. M.; Friend, R. H.; Millard, I. S.; Lacey, D. J.; Butler, T.; Burroughes, J. H.; Cacialli, F. *J. Appl. Phys.* **2003**, *93*, 6159.
43. Cappel, U. B.; Feldt, S. M.; Schöneboom, J.; Hagfeldt, A.; Boschloo, G. The Influence of Local Electric Fields on Photoinduced Absorption in Dye-Sensitized Solar Cells. *J. Am. Chem. Soc.* **2010**, *132*, 9096–9101.
44. Luther, J. M.; Jain, P. K.; Ewers, T.; Alivisatos, A. P. Localized Surface Plasmon Resonances Arising from Free Carriers in Doped Quantum Dots. *Nat. Mater.* **2011**, *10*, 361–6.
45. Perner, M.; Bost, P.; Lemmer, U.; Plessen, G. v.; Feldmann, J. Optically Induced Damping of the Surface Plasmon Resonance in Gold Colloids. *Phys. Rev. Lett.* **1997**, *78*, 2192–5.
46. Ginger, D. S.; Greenham, N. C. Charge Injection and Transport in Films of CdSe Nanocrystals. *J. Appl. Phys.* **2000**, *87*, 1361.
47. Morgan, N. Y.; Leatherdale, C. A.; Drndić, M.; Jarosz, M. V.; Kastner, M. A.; Bawendi, M. Electronic Transport in Films of Colloidal CdSe Nanocrystals. *Phys. Rev. B* **2002**, *66*, 075339.
48. Lombardo, C. J.; Akhavan, V. A.; Panthani, M. G.; Goodfellow, B. W.; Korgel, B. A.; Dodabalapur, A. Temperature-dependent charge transport in copper indium diselenide nanocrystal films. *J. Appl. Phys.* **2012**, *111*, 073703.
49. Kruszynska, M.; Borchert, H.; Parisi, J.; Kolny-Olesiak, J. Synthesis and Shape Control of $CuInS_2$ Nanoparticles. *J. Am. Chem. Soc.* **2010**, *132*, 15976–15986.
50. Sheng, X.; Wang, L.; Luo, Y.; Yang, D. Synthesis of hexagonal structured wurtzite and chalcopyrite $CuInS_2$ via a simple solution route. *Nano. Res. Lett.* **2011**, *6*, 562.
51. Kahn, A.; Koch, N.; Gao, W. Electronic Structure and Electrical Properties of Interfaces between Metals and $\pi$-Conjugated Molecular Films. *J. Polym. Sci., Part B: Polym. Phys.* **2003**, *41*, 2529–2548.
52. Ehrler, B.; Musselman, K. P.; Bohm, M. L.; Morgenstern, F. S. F.; Vaynzof, Y.; Walker, B. J.; MacManus-Driscoll, J. L.; Greenham, N. C. Preventing Interfacial Recombination in Colloidal Quantum Dot Solar Cells by Doping the Metal Oxide. *ACS Nano* **2013**, *7*, 4210–4220.